

Stochastic 3D modeling of the microstructure of lithium-ion battery anodes via Gaussian random fields on the sphere

Feinauer, Julian^{a,b,*}, Brereton, Tim^b, Spettl, Aaron^b, Weber, Matthias^b, Manke, Ingo^c, Schmidt, Volker^b

^a*Deutsche ACCUmotive GmbH & Co. KG, Kirchheim unter Teck*

^b*Institut für Stochastik, Universität Ulm*

^c*Helmholtz-Zentrum Berlin*

Abstract

The performance and durability of lithium-ion batteries are highly dependent on the microstructures of their components. Recently, methods have been developed that make possible the simulation of electrochemical processes on 3D representations of lithium-ion batteries. However, it is difficult to obtain realistic microstructures on which these simulations can be carried out. In this paper, we develop a stochastic model that is able to produce realistic microstructures of lithium-ion battery anodes, which can serve as input for the simulations. We introduce the use of Gaussian random fields on the sphere as models for the particles that form the anodes. Using this new approach, we are able to model realistic particle geometries. The stochastic model also uses a number of techniques from stochastic geometry and spatial statistics. We carry out validation of our model, in order to demonstrate that it realistically describes the key features of the anode's microstructure.

Keywords: Stochastic 3D microstructure modeling, Lithium-ion cell anodes, Gaussian random fields, Spherical harmonics;

1. Introduction

Lithium-ion batteries used in electric vehicles need to fulfill a number of requirements. They should charge quickly, especially at low temperatures, be highly durable under a wide range of climatic conditions, and provide sufficient

*Corresponding author

Email address: julian.feinauer@daimler.com (Feinauer, Julian)

energy storage capabilities for long driving ranges [1]. A number of challenges remain, however, in satisfying these requirements. These are largely due to the complex nature of the batteries' microstructures. For example, lithium plating can occur at low temperatures; see [2, 3, 4, 5]. This is caused by the slow transport of lithium ions in the electrolyte and bulk material, which is a direct result of the geometry of the microstructure; see [6, 7]. Cyclic aging is also related to the microstructure; see, e.g., [8, 5, 9]. The influence of different operating conditions on cell degradation has been studied using electrochemical principles; see, e.g., [10, 7]. Much of this research has made use of 1D or pseudo-2D models developed by Newman and co-workers [7]. For example, aging has been studied in [11] and lithium plating has been studied in [10] and [12]. However, these models do not fully take into account the importance of the microstructure and use only averaged structural characteristics like tortuosity, volume fraction and mean particle radius. Recent research, however, shows that the microstructure plays a key role in determining functional characteristics of the material; see, e.g., [13, 14].

Recently, significant advances have been made in the simulation of electrochemical processes in 3D models of lithium-ion batteries [15, 16, 6, 17, 18]. Using these simulations, it is possible to carry out detailed studies of the relationships between the morphologies of battery materials and their corresponding transport behaviors. This approach has proven very effective in studying other energy materials, such as fuel cells; see, e.g., [19, 20]. Important processes such as degradation can also be investigated and connected to the properties of the materials. A limitation of these simulation based approaches, however, is that it is very difficult to obtain realistic 3D microstructure models to use as input. This is because the small scales make 3D imaging of sufficiently large and representative material samples very difficult; see [21, 22, 23, 24, 25]. In addition, it would be desirable to investigate realistic microstructures that do not correspond to materials that have already been physically produced [26].

Stochastic modeling has proved to be a very effective method of producing realistic microstructures without the need for microscopy or computationally expensive physics-based simulations; see, e.g., [27, 28, 29, 30, 31, 32, 33, 34, 35]. Stochastic models have also been successfully coupled with numerical simulations; see, e.g., [28, 36, 37]. Using fast and flexible stochastic models, it is then possible to investigate the relationships between microstructure characteristics and material functionality [38].

In this paper, we develop a stochastic model for the microstructure of lithium-ion battery anodes, which consists of a network of connected graphite particles. The model uses a number of techniques from stochastic geometry and spatial statistics; see, e.g., [39, 40, 41]. As a major innovation, it introduces the use of Gaussian random fields on the sphere to model particle shapes. In most standard approaches, particles are described by simple geometric objects such as balls and ellipsoids. However, the particles we consider are not adequately described by such shapes [42, 43]. Using spherical harmonics expansions of Gaussian random fields, we are able to represent particles with much more complex shapes [44, 42].

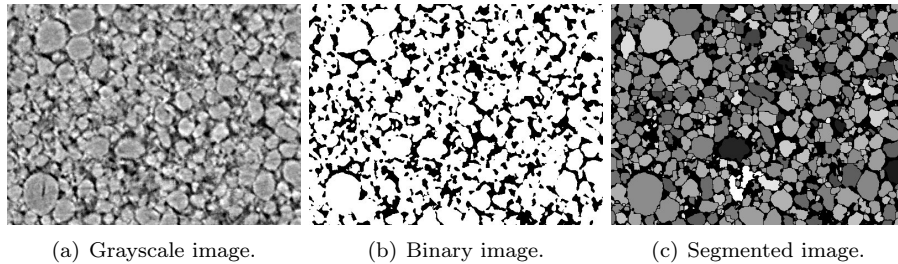


Figure 1: 2D cutout of experimental data.

Our stochastic model uses a random tessellation to roughly describe the shape, size and position of the particles. A random graph is then used to describe how the particles connect with one another, in order to replicate the connectivity structure of the material itself. Using the tessellation and the connectivity graph, the particles themselves are produced. We exploit properties of Gaussian random fields to force the particles to connect in the desired manner. In the final step, the structure is morphologically smoothed to resemble the empirical microstructures as closely as possible.

The paper has the following structure. We first briefly describe the material and the methods by which we image it and extract its microstructure. We then describe the stochastic model itself. Afterward, we carry out validation of the model, by considering a number of important microstructure characteristics. In the last section, we provide a summary of the paper and describe future research that we will carry out.

2. Experimental data

The experimental data in this paper consists of four samples that are extracted from a large scale lithium-ion battery used in automotive applications. The cell did not contain electrolyte in order to ensure that the microstructure of the anode was not altered by electrical operation. The cell was disassembled and four samples were extracted from different positions and layers in the cell. This was done to ensure that the samples were as reflective as possible of the material's structure; see [23]. The obtained image data is shown in Figure 1 alongside the binarized and segmented versions.

2.1. Description of samples & imaging technique

The 3D data sets were created at the Synchrotron X-ray imaging facility BAMLine at BESSY (Berlin, Germany). The setup consists of a PCO4000 detector system with 4008×2672 pixels and an optical system (Optique Peter) with a CWO scintillator screen that was used to convert X-rays into visible light. An X-ray energy of 19 keV was used. The pixel size was about $0.44 \mu\text{m}^2$. During the tomographic measurement, 2200 single radiographic projections were taken

at equidistant angles over a range of 180° . A filtered back-projection algorithm was used for 3D data reconstruction.

Details on the measurement and on the sample preparation method that was used to minimize the differences in the samples induced by varying measurement conditions are described in [23]. After imaging and reconstruction, the sample data is in the form of four 3D images, each $2097 \times 828 \times 119$ voxels. Each voxel has a grayscale value, which ranges from 0 to 255.

2.2. Structural segmentation

A graphite electrode comprises a fully connected network of particles. In order to extract information about the individual particles from the image data, we carry out a structural segmentation procedure consisting of four steps: (1) we binarize the original grayscale image; (2) we remove holes within the particles; (3) we remove irregularities such as parts extruding from the surfaces of the particles; (4) we segment the image into separate particles using a watershed procedure.

In the binarization step, we allocate each voxel to either the solid (graphite) phase or to the pore space. We first apply a Gaussian filter with $\sigma = 1.0$ in order to reduce the noise in the image data. We then use a global threshold to produce a binarized image. More precisely, every voxel with a grayscale value greater than or equal to 32 is assigned to the solid phase and every voxel with a value less than 32 is assigned to the pore phase; see [45] for more details. The threshold value is chosen to reproduce the volume fraction of the solid phase, which is known to be 73% for this material.

In the second step, we remove holes within the solid phase in order to avoid over-segmentation which would otherwise occur; see [46]. These holes are mainly caused by artifacts in the imaging and thresholding procedures. The particles themselves should not contain holes. We remove the holes using a Hoshen-Kopelman clustering algorithm (see [47]) on the pore phase of the thresholded image. Every cluster consisting of less than 5000 pore space voxels is removed by relabeling all the member voxels as belonging to the solid phase. The threshold of 5000 was chosen to ensure that hollow regions within particles were removed, but isolated pores still remained.

We then remove regions where the pore space intrudes significantly into the particles. The procedure is as follows. We generate a one voxel thick skeletonization of the pore phase. The skeleton, S_1 , is generated using Lee thinning [48]. The ‘dead-end’ branches of S_1 , which are only connected at one end, represent intrusions into the solid phase. We generate a second skeleton, S_2 , which is simply S_1 with the ‘dead-end’ branches removed. We remove the intrusions by reassigning to the solid phase all voxels in the pore space that are closer to S_1 than S_2 .

In the last step, the four binary images are segmented into disjoint parts, with each part containing only one particle. The segmentation is performed for each binary image using a marker watershed algorithm as in [49, 50]. In order to calculate the positions of the markers, we first calculate a distance transform

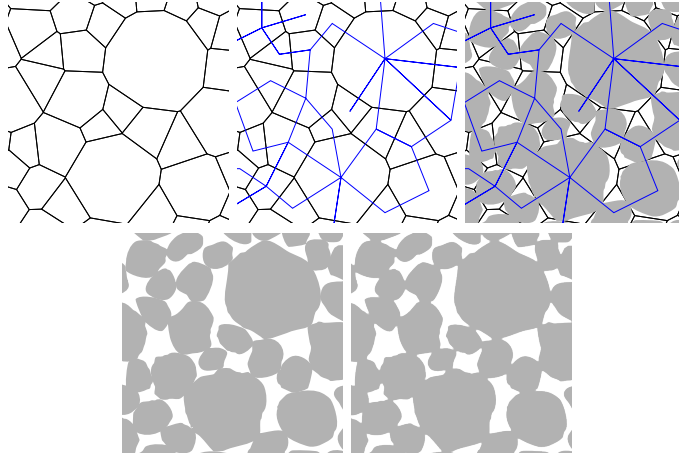


Figure 2: Schematic depiction of the stochastic model. 1. A random tessellation is produced, which roughly determines the particle shapes, sizes and locations. 2. A random graph describes how the particles connect. 3. The connected particles are produced using Gaussian random fields on the sphere. 4 and 5. The connected particles are retained and morphological smoothing is carried out.

of each binary image. This results in a transformed image, D , where each voxel is assigned its (minimum) distance from the pore phase, with voxels belonging to the pore phase being assigned a value of 0. We then consider the reflection of the distance transformed image, $\tilde{D} = -D$. For each image, we take the local minima of \tilde{D} as potential markers to use in the watershed transform. However, because there is still a risk of over-segmentation — due, for example, to slightly cracked particles — we take only a subset of these local minima as markers, using the method described in [51]. The segmentation is then performed on the distance transformed image \tilde{D} using this subset of markers.

3. Stochastic 3D model of the microstructure

We model the solid phase of the anode using a connected network of irregular particles. The modeling procedure consists of four distinct steps: (1) the positions of the particles are determined using a random tessellation; (2) a graph is generated, conditional on the tessellation, that describes the connectivity between particles; (3) the particles themselves are modeled as Gaussian random fields on the sphere, whose properties depend on the tessellation and connection graph; and, (4) morphological smoothing is performed on the simulated particle system. A schematic description of the modeling procedure is shown in Figure 2.

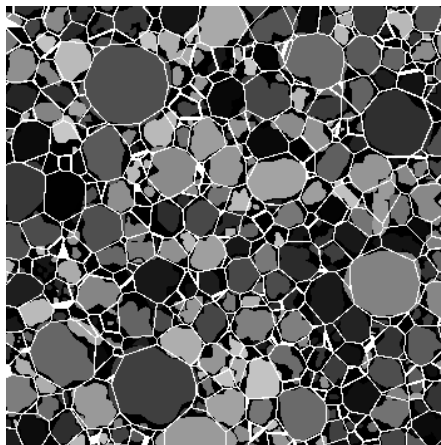


Figure 3: A Laguerre diagram fitted to a 2D cutout of the experimental data set. The generating particles are also shown.

3.1. Determining the locations of the particles

The particles in the material are densely packed, with a volume fraction of 73%. In order to ensure that the stochastic model produces similarly dense configurations, we use a random tessellation to partition the space into cells. We then place a particle in each cell. The size and shape of each particle is largely determined by the geometry of its corresponding cell. In particular, the expected volume of a particle is equal to 73% of the corresponding cell's volume. In this manner, we are able to achieve tightly packed configurations of particles with realistic volume fractions. As it transpires, random tessellations based on Laguerre diagrams can describe the shape, size and location of the particles very well.

A Laguerre diagram in the d -dimensional Euclidean space \mathbb{R}^d (in particular, for $d = 2$ and $d = 3$) is defined by a sequence of marked points, $\varphi = \{(x_i, r_i)\}$, where the $x_i \in \mathbb{R}^d$ and the $r_i \in [0, \infty)$. It partitions the space \mathbb{R}^d into cells such that the cell associated with the j th marked point, (x_j, r_j) , is given by

$$C_j = C((x_j, r_j), \varphi) = \{y \in \mathbb{R}^d : d_L(y, (x_j, r_j)) \leq d_L(y, (x', r')), (x', r') \in \varphi\},$$

where $d_L(y, (x, r)) = \|y - x\|^2 - r^2$, with $\|\cdot\|$ the Euclidean norm in \mathbb{R}^d . Under suitable regularity conditions on φ (see [52]), this will define a tessellation. For more details on Laguerre tessellations, see [52, 53].

When describing the empirical data using a Laguerre diagram, an obvious choice of the x_i is the centroids of the particles. Likewise, the r_i can be taken to be the equivalent radii of the particles. That is, the radii of spheres with the same volumes. Figure 3 shows a 2D cutout of a Laguerre diagram fitted to one of the empirical data sets. Note that the sizes and shapes of the particles are closely related to the geometry of their corresponding cells.

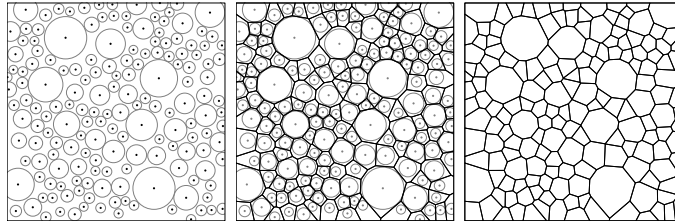


Figure 4: Generating the random tessellation. 1. The marked point process is generated. 2. The tessellation is generated by the marked points. 3. The points are discarded and the tessellation is retained.

A random tessellation in \mathbb{R}^3 with properties very close to those of the tessellations produced by the empirical data can be produced using a version of a random sequential adsorption (RSA) process (see [39] and [41] for details). This results in a random marked point process, φ , which is generated sequentially in a bounded window, $W \subset \mathbb{R}^3$, using an acceptance-rejection approach. This continues until a stopping condition is met. The procedure is as follows:

1. Set $\varphi = \emptyset$.
2. Generate a proposal point, (\tilde{x}, \tilde{r}) , with \tilde{x} distributed uniformly in W and \tilde{r} sampled from a gamma distribution with shape parameter α and rate parameter β .
3. Add the point (\tilde{x}, \tilde{r}) to the point set φ if the ball centered at \tilde{x} with radius \tilde{r} does not overlap with the ball of any point already in φ . That is, set $\varphi = \varphi \cup \{(\tilde{x}, \tilde{r})\}$ if

$$\bigcup_{(x', r') \in \varphi} (B_{\tilde{r}}(\tilde{x}) \cap B_{r'}(x')) = \emptyset,$$

where $B_r(x) = \{y \in \mathbb{R}^3 : \|y - x\| < r\}$ with $\|\cdot\|$ the Euclidean norm.

4. If the fraction of W covered by the balls is larger than v_f or there is no possibility to add another ball with minimal radius r_l without overlapping the balls of existing points, then stop. Otherwise, repeat from step 2.

The RSA process has three parameters: α , β and v_f . These are chosen so that the resulting tessellations resemble the tessellations extracted from the empirical data as closely as possible. We consider a vector $\mathbf{q} = (q_1, \dots, q_6)$ of tessellation characteristics: q_1 , the mean volume of the cells; q_2 , the variance of the volumes of the cells; q_3 , the mean surface area of the cell faces; q_4 , the variance of the surface areas of the cell faces; q_5 , the mean number of faces of each cell; and q_6 , the variance of the mean numbers of faces of each cell. We estimate these characteristics for each of the four empirical data sets. We then take pointwise averages to get an estimate of the empirical tessellation

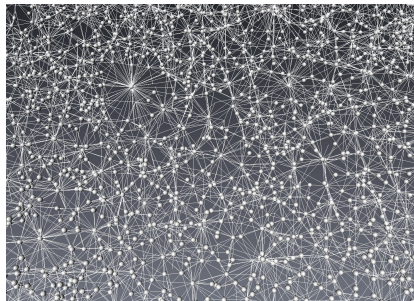


Figure 5: A graph showing how particles are connected to one another in one of the empirical data sets.

characteristics, $\hat{\mathbf{q}}^E$. In order to calculate the corresponding characteristics for the point process with parameter constellation (v_f, α, β) , we first produce a realization of the marked point process with these parameters in a window $W = [0, 2000] \times [0, 2000] \times [0, 120]$. We then estimate the characteristics of the tessellation produced by this point process, resulting in a vector $\hat{\mathbf{q}}^{(v_f, \alpha, \beta)}$. The parameters of the RSA process are chosen to minimize the cost function

$$L(v_f, \alpha, \beta) = \sqrt{\sum_{i=1}^6 \left(\frac{\hat{q}_i^E - \hat{q}_i^{(v_f, \alpha, \beta)}}{\hat{q}_i^E} \right)^2}.$$

The minimization is carried out using the Nelder-Mead algorithm, with initial parameters $v_f^0 = 0.230$, $\alpha^0 = 2.217$ and $\beta^0 = 0.312$. The initial parameters were chosen using a preliminary optimization step, where the RSA process parameters were fitted to key characteristics of the empirical marked point patterns. The final parameters for the tessellation model are given by $(\hat{v}_f, \hat{\alpha}, \hat{\beta}) = (0.231, 2.329, 0.1988)$. The procedure for generating the random tessellation is illustrated in Figure 4. Note that the RSA process is subject to edge effects. However, these can be removed by, e.g., plus sampling; see [39].

3.2. Connectivity Graph

The particles in the anode form a connected system. The connectivity relations of the empirical data sets are extracted by treating two particles as connected if voxels from one particle directly neighbor voxels from the other particle. Figure 5 shows a graph of the connectivity relationship in one of the samples. It is clear that the particles are connected in a highly complex manner. We model the connectivity relations using a random graph, $G_c = (V_c, E_c)$; see also [54, 55]. The vertices of the graph, V_c , correspond to the cells of the Laguerre tessellation generated above. The edges of the graph, E_c , designate which particles will be connected to one another. For this reason, we only allow edges to be placed between vertices whose corresponding tessellation cells have a common face.

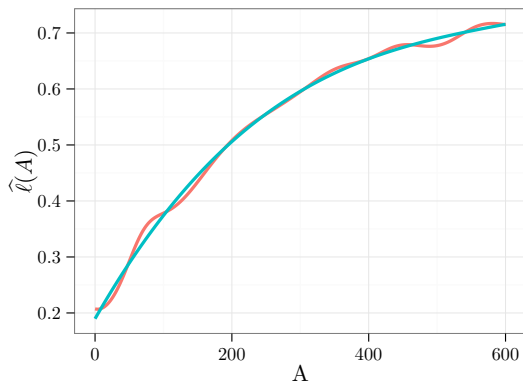


Figure 6: Estimate of $\hat{\ell}(A)$, the probability two particles with a separating tessellation face of area A are connected. Black: estimated probability $\hat{\ell}(A)$; blue: approximating function given in (3.1).

In order to ensure that the particles form a single connected component, we use a minimal spanning tree as the basis of the connectivity graph. We generate the minimal spanning tree as follows. We consider the graph containing every possible edge (i.e., where all neighboring particles are connected to one another). For each pair of vertices, i and j , such that there is a possible edge, we weight the edge by $1/A_{i,j}$, where $A_{i,j}$ is the surface area of the face of the tessellation separating the two corresponding cells. We then calculate the minimal spanning tree of this weighted graph, resulting in a fully connected graph with a small number of edges.

We add additional edges to G_c so that the connectivity structure resembles that of the material. To do this, we consider each potential edge separately. It turns out that the probability of two neighboring particles, i and j , being connected is directly related to $A_{i,j}$. Figure 6 shows an estimate, $\hat{\ell}(A)$, of the probability two particles are connected given the surface area of the face of the tessellation separating them is A . This is a conditional probability of the form

$$\ell(A) = \mathbb{P}(\text{particles } i \text{ and } j \text{ are connected} \mid A_{i,j} = A).$$

The probability is estimated from the data using the estimator

$$\hat{\ell}(A) = \frac{\hat{f}(A_{i,j} = A \mid \text{particles } i \text{ and } j \text{ are connected})}{\hat{f}(A_{i,j} = A)} \cdot \frac{N_C}{N_T},$$

where N_C is the number of pairs of connected particles in the experimental tessellations, N_T is the total number of faces in the experimental tessellations, and $\hat{f}(B)$ is a kernel density estimate of the density of faces with property B . Choosing an appropriate approximating function, we have

$$\ell(A) \approx \min(c_1 A^3 + c_2 A^2 + c_3 A + c_4, 1). \quad (3.1)$$

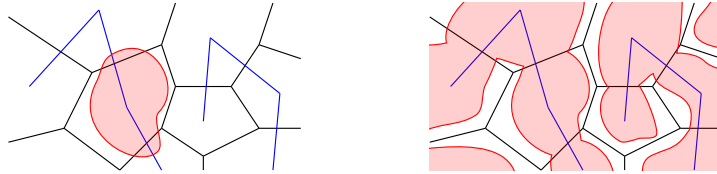


Figure 7: Generating the particle network. Left: particles are created by simulating Gaussian random fields on the sphere inside each tessellation cell. Right: as the particles are simulated, they are forced to connect according to the graph G_c (shown in blue).

The coefficients of the polynomial are fitted via non-linear least squares using the Gauss-Newton algorithm, obtaining $c_1 = 1.714 \cdot 10^{-9}$, $c_2 = -3.133 \cdot 10^{-6}$, $c_3 = 2.140 \cdot 10^{-3}$ and $c_4 = 1.897 \cdot 10^{-1}$. Figure 6 shows the approximating function gives an excellent fit to $\widehat{\ell}(A)$.

3.3. Generating the particles

Given the tessellation and the connection graph, we are able to generate the particle network itself. We first place a particle inside each cell of the tessellation. The individual particles are realizations of isotropic Gaussian random fields on the sphere. We use Gaussian random fields as they provide enormous flexibility in modeling particle shapes, are easily implemented, and can be adapted to produce a network of connected particles. We consider random fields, $\psi : [0, \pi] \times [0, 2\pi) \rightarrow \mathbb{R}$, that are completely characterized by a mean radius, μ , and an angular power function, $A : [0, \infty) \rightarrow [0, \infty)$. The value $\psi(\theta, \phi)$ describes the distance from the centroid of a particle to its surface in direction (θ, ϕ) . The mean radius controls the size of a particle and the angular power function controls its shape. We choose a common angular power function to describe the shape of all the particles and mean radii that ensure the particle system has the desired volume fraction. Approximate realizations of the Gaussian random fields are then generated by simulating multivariate normal random vectors. We are able to use the properties of the multivariate normal distribution, combined with the information from the connectivity graph, G_c , to ensure that the particles are connected as desired. The basic idea of this step of our modeling approach is illustrated in Figure 7. Note that, although it is possible that the Gaussian random field may take negative values, we choose the coefficients of our model so that this occurs with negligible probability. If, by chance, a random field with negative values is generated, we discard it and generate a new particle.

3.3.1. Isotropic Gaussian random fields on the sphere

For $l \in \{0, 1, \dots\}$ and $m \in \{0, 1, \dots, l\}$, we define the spherical harmonic function, $Y_{l,m} : [0, \pi] \times [0, 2\pi) \rightarrow \mathbb{C}$, by

$$Y_{l,m}(\theta, \phi) = \sqrt{\frac{2l+1}{4\pi} \frac{(l-m)!}{(l+m)!}} P_{l,m}(\cos(\theta)) e^{im\phi}, \quad l \in \{0, 1, \dots\}, m \in \{0, 1, \dots, l\},$$

where $P_{l,m}(u)$ is the associated Legendre function; see [56]. The angular power function defines an angular power spectrum, $(A_l)_{l=0}^{\infty}$, by $A_l = A(l)$ for $l \in \{0, 1, \dots\}$. An isotropic Gaussian random field on the sphere, ψ , with mean radius μ and angular power spectrum $(A_l)_{l=0}^{\infty}$, can be represented in terms of spherical harmonic functions by the infinite sum

$$\psi(\theta, \phi) = \sum_{l=0}^{\infty} \left[a_{l,0} Y_{l,0}(\theta, \phi) + 2 \sum_{m=1}^l [\operatorname{Re}(a_{l,m}) \operatorname{Re}(Y_{l,m}(\theta, \phi)) + \operatorname{Im}(a_{l,m}) \operatorname{Im}(Y_{l,m}(\theta, \phi))] \right], \quad (3.2)$$

where

$$a_{0,0} \sim \mathcal{N}(\mu, A_0), a_{l,0} \sim \mathcal{N}(0, A_l) \text{ for } l > 0,$$

and

$$\operatorname{Re}(a_{l,m}) \sim \mathcal{N}(0, A_l/2) \text{ and } \operatorname{Im}(a_{l,m}) \sim \mathcal{N}(0, A_l/2) \text{ for } l, m > 0;$$

see [56]. In practice, we truncate (3.2) so that we have

$$\psi(\theta, \phi) \approx \sum_{l=0}^L \left[a_{l,0} Y_{l,0}(\theta, \phi) + 2 \sum_{m=1}^l [\operatorname{Re}(a_{l,m}) \operatorname{Re}(Y_{l,m}(\theta, \phi)) + \operatorname{Im}(a_{l,m}) \operatorname{Im}(Y_{l,m}(\theta, \phi))] \right].$$

We can then write the $a_{l,0}$, $l \in \{1, \dots, L\}$ and the real and imaginary components of $a_{l,m}$, $m \in \{1, \dots, l\}$, $l \in \{1, \dots, L\}$, in a vector as

$$\mathbf{a} = (a_{0,0}, a_{1,0}, \operatorname{Re}(a_{1,1}), \operatorname{Im}(a_{1,1}), a_{2,0}, \operatorname{Re}(a_{2,1}), \operatorname{Im}(a_{2,1}), \operatorname{Re}(a_{2,2}), \dots, \operatorname{Im}(a_{L,L}))^\top, \quad (3.3)$$

with $\mathbf{a} \sim \mathcal{N}(\boldsymbol{\mu}, \Sigma)$, where $\boldsymbol{\mu} = (\mu, 0, \dots, 0)$ and

$$\Sigma = \operatorname{diag}(A_0, A_1, A_1/2, A_1/2, A_2, A_2/2, A_2/2, A_2/2, \dots, A_L/2, A_L/2).$$

We will denote the components of \mathbf{a} by a_1, \dots, a_M , where $M = (L+1)^2$. The spherical harmonics functions can also be written in vector form as

$$\mathbf{y}^{(\theta, \phi)} = (Y_{0,0}(\theta, \phi), Y_{1,0}(\theta, \phi), 2 \cdot \operatorname{Re}(Y_{1,1}(\theta, \phi)), \dots, 2 \cdot \operatorname{Re}(Y_{L,L}(\theta, \phi)), 2 \cdot \operatorname{Im}(Y_{L,L}(\theta, \phi)))^\top,$$

with the components of $\mathbf{y}^{(\theta, \phi)}$ denoted by $y_1^{(\theta, \phi)}, \dots, y_M^{(\theta, \phi)}$. The Gaussian random field, ψ , is thus approximated by

$$\psi(\theta, \phi) \approx \mathbf{a}^\top \mathbf{y}^{(\theta, \phi)} = \sum_{k=1}^M y_k^{(\theta, \phi)} a_k. \quad (3.4)$$

Using this formulation, we can simulate an approximation of an isotropic Gaussian random field on the sphere by generating a multivariate normal random vector of length M . For all numerical calculations in this paper we use $L = 14$.

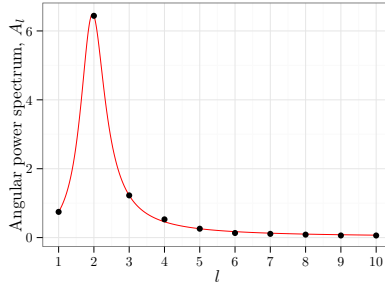


Figure 8: The fitted angular power function. Black points: empirical estimates of the angular power spectrum; red line: estimated angular power function.

3.3.2. Determining the angular power function

The shapes of the particles are determined by the angular power function $A : [0, \infty) \rightarrow [0, \infty)$. Because we use truncations to approximate the Gaussian random fields by sums involving only M terms, we wish to use an angular power function that is able to describe the shapes of the particles in the experimental data but also goes to zero quickly. A suitable choice is a rational function of the form

$$A(l) = \frac{al + b}{l^2 + cl + d}. \quad (3.5)$$

In order to fit this function, we consider every particle in the four experimental samples. For each particle, we compute the vector of coefficients given in (3.3). This is done using the procedure introduced in [42]. By calculating the sample variances of appropriately scaled versions of these coefficients, we get estimates, $\hat{A}_0, \dots, \hat{A}_M$ of A_0, \dots, A_M . We then find the coefficients of (3.5) via non-linear least squares using the Levenberg-Marquard algorithm; see [57]. The estimated coefficients are $a = 0.4241$, $b = 0.356$, $c = -3.858$ and $d = 3.903$ with $R^2 = 0.98$. Figure 8 shows the estimated angular power function. Note that it decays to zero quickly, justifying our use of the truncated sum, (3.4), to simulate the Gaussian random fields.

3.3.3. Describing individual particles by Gaussian random fields

We use the same angular power function for each particle. However, every individual particle has a centroid and a mean radius that are determined by the geometry of the corresponding cell in the tessellation generated in Section 3.1. For the i th particle, we choose the centroid, c_i , to be the barycenter of all the vertices of its cell C_i .

In order to sufficiently control the volume of the particles so as to ensure that the volume fraction of the particle system is correct, it is necessary to replace the normally distributed first spherical harmonic coefficient, a_1 , by a constant. This constant is calculated by noting that the expected volume of a particle,

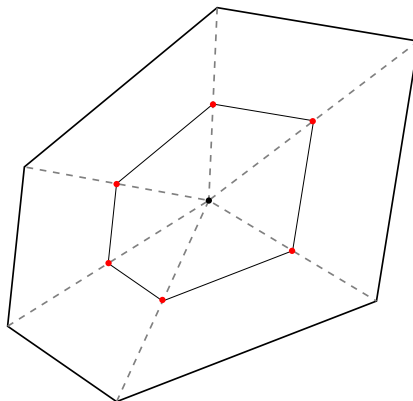


Figure 9: The points on the face of a tessellation cell that the random field must touch.

when using the angular power function determined in Section 3.3.2, is given by

$$\mathbb{E}V \approx 0.09403a_1^3 + 4.34444a_1.$$

We select the a_1 value for each particle to be such that the expected volume of the particle is 0.73ρ of the volume of its corresponding cell in the Laguerre tessellation, where ρ is an adjustment factor introduced to compensate for the effects of morphological smoothing and particles overlapping. Using the minimum contrast method, this factor was found to be 0.9251.

3.3.4. Determining the constraints on the particle shapes

We are able to generate particles with the desired shapes and locations using the specified angular power function, mean radii and particle centroids. However, the particles will not be connected to each other in the manner described by G_c . We resolve this issue by first determining, for each particle, a set of points that it should touch. These points translate into constraints on the spherical harmonics coefficients, which ensure points connect in the manner we intend.

We determine the points that the i th particle must touch as follows. We consider the set $\mathcal{N}_i = \{j \in V_c : i \neq j, (i, j) \in E_c\}$. This represents the particles with which the i th particle should connect, as determined by G_c . Corresponding to each of these particles is a face in the Laguerre tessellation. Let $F_{i,j}$ be the face in the tessellation separating particles i and j . For each $F_{i,j}, j \in \mathcal{N}_i$, we define a set of points the particle must touch. We place points a fixed proportion, 0.15, of the distance from the centroid of $F_{i,j}$ to each of its vertices. This procedure is illustrated in Figure 9. We then express these points in spherical coordinates, (θ, ϕ, r) , with the origin being the centroid of the i th Laguerre cell. Thus, for the i th particle, we get a sequence of points, $(\theta_1, \phi_1, r_1), \dots, (\theta_{n_i}, \phi_{n_i}, r_{n_i})$, that the particle must touch.

3.3.5. Generating the particles conditional on the constraints being satisfied

We generate each particle's spherical harmonics coefficient vector, \mathbf{a} , from a multivariate normal distribution conditioned on the points $(\theta_1, \phi_1, r_1), \dots, (\theta_{n_i}, \phi_{n_i}, r_{n_i})$ being touched. Using (3.4), we can write each of the constraints as a linear equation

$$\sum_{k=1}^M y_k^{(\theta_j, \phi_j)} a_k = r_j, \quad j = 1, \dots, n_i.$$

Because we treat a_1 as constant for each particle, we rewrite this equation with only random quantities on the left hand side, to get

$$\sum_{k=2}^M y_k^{(\theta_j, \phi_j)} a_k = r_j - a_1 Y_1^{(\theta_j, \phi_j)}, \quad j = 1, \dots, n_i.$$

Writing this system of equations in matrix form, we obtain

$$Y \cdot \tilde{\mathbf{a}} = \tilde{\mathbf{r}}, \quad (3.6)$$

where $\tilde{\mathbf{a}} \sim \mathcal{N}(\mathbf{0}, \tilde{\Sigma})$, with $\tilde{\Sigma} = \text{diag}(A_1, A_1/2, \dots, A_L/2)$. The matrix Y admits the singular value decomposition $Y = USV^\top$, where U and V are orthogonal matrices and $S = \text{diag}(\sigma_1, \dots, \sigma_s, 0, \dots, 0)$, with $s = \text{rk}(Y)$ and $\sigma_1, \dots, \sigma_s$ the singular values of Y . Using the singular value decomposition, we rewrite (3.6) as $USV^\top \tilde{\mathbf{a}} = \tilde{\mathbf{r}}$ which allows us to write $SV^\top \tilde{\mathbf{a}} = U^\top \tilde{\mathbf{r}}$, with $V^\top \tilde{\mathbf{a}} \sim \mathcal{N}(\mu_{V^\top \tilde{\mathbf{a}}}, \Sigma_{V^\top \tilde{\mathbf{a}}})$. The boundary conditions can then be written as

$$(V^\top \tilde{\mathbf{a}})_i = \sigma_i^{-1} U^\top \tilde{\mathbf{r}}, \quad i = 1, \dots, s.$$

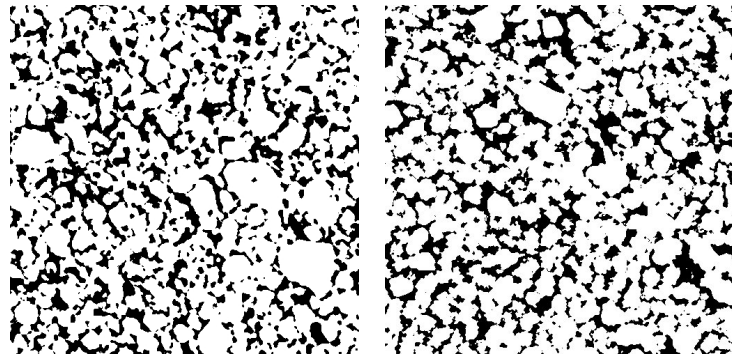
Thus, we can impose the boundary conditions by drawing $(V^\top \tilde{\mathbf{a}})_{i=s+1}^M$ from a $\mathcal{N}(\mu_{V^\top \tilde{\mathbf{a}}}, \Sigma_{V^\top \tilde{\mathbf{a}}})$ distribution conditional on $\{(V^\top \tilde{\mathbf{a}})_1 = \sigma_1^{-1} U^\top \tilde{\mathbf{r}}, \dots, (V^\top \tilde{\mathbf{a}})_s = \sigma_s^{-1} U^\top \tilde{\mathbf{r}}\}$. Having generated the random vector, $V^\top \tilde{\mathbf{a}}$, which is conditioned on the boundary conditions being satisfied, we obtain the vector of spherical harmonics coefficients, \mathbf{a} , by setting $\mathbf{a} = VV^\top \tilde{\mathbf{a}}$.

3.4. Morphological Smoothing

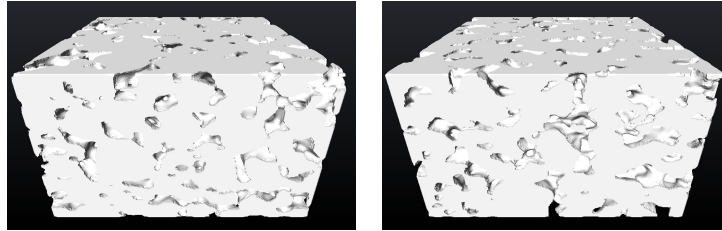
The particles in the material are actually encased in a thin layer of binder. However, the volume fraction of this binder is too small to be modeled directly. Instead, we carry out morphological smoothing, which mimics this effect. In particular, it smooths the sharp edges around particle connections. The morphological smoothing is performed using a ball with radius 1 as the structuring element, where the union set of particles is first dilated, then eroded. For more details on the procedure, see [58].

4. Validation

Figure 10 shows 2D and 3D cutouts from the experimental data alongside cutouts from a realization of the stochastic model. On the surface, the experimental and simulated microstructures appear to have very similar characteristics. In order to ensure that these characteristics are indeed sufficiently close, we



(a) 2D cutout of the experimental data. (b) 2D cutout of a simulated structure.



(c) 3D cutout of the experimental data. (d) 3D cutout of a simulated structure.

Figure 10: 2D and 3D cutouts of the experimental and simulated microstructures.

	Experimental	Simulated	Relative Error
Volume Fraction	0.734	0.732	0.225 %
Specific Surface Area (voxel^{-1})	303842.2	299305	1.493 %
Mean Tortuosity of Pore Space	1.577	1.569	0.517 %

Table 1: Characteristics describing the particle system.

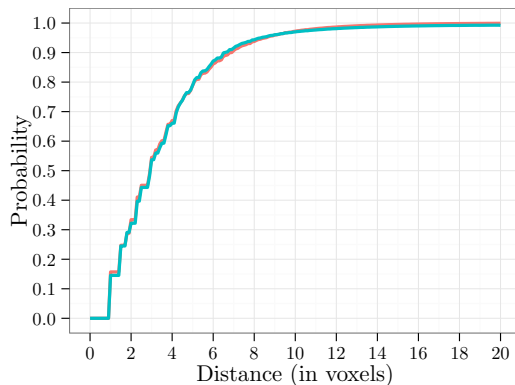


Figure 11: The spherical contact distribution functions for the experimental and stochastic microstructures. Red: experimental; blue: simulated.

carry out an extensive validation. We compare a number of key characteristics of the microstructures produced by the stochastic model with those of the structures extracted from the empirical data. All the characteristics we consider are estimated directly from binary images of dimension $500 \times 500 \times 119$. In the case of the experimental data, 50 such images are sampled uniformly from the larger images. In the case of the stochastic model, 50 realizations of the stochastic model are generated in windows of the appropriate size.

The characteristics we consider include both standard characteristics used in the evaluation of microstructures, see, e.g., [39, 41], and characteristics that play key roles in determining the functionality of lithium-ion batteries; see, e.g. [33, 34]. We first compute characteristics for the solid phase. Then, we consider characteristics for the pore phase, as these play an important role in determining the transport properties of the material.

4.1. Characteristics of the solid phase

We begin by considering a number of first order characteristics describing the microstructure the particle system. These are given in Table 1. The average volume fraction of the simulated particle systems is, as expected, close to that observed in the experimental data. Likewise, the specific surface areas of the particle systems are very similar. The mean tortuosities of paths through pores of the particle network are also very close to one another.

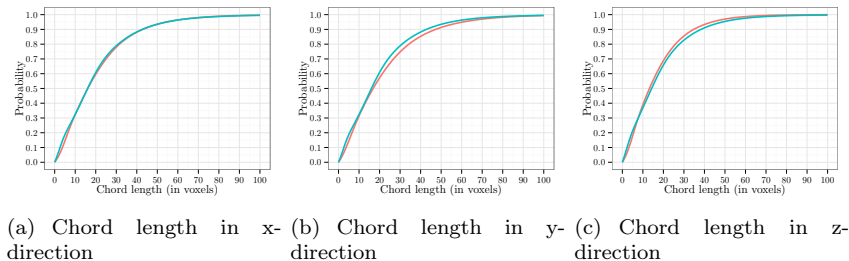


Figure 12: Chord length distribution functions in the x , y and z directions. Red: experimental; blue: simulated.

A more detailed description of the geometry of the solid phase is given by the spherical contact distribution function. This gives the probability that the distance from a randomly chosen voxel of the pore space to a voxel of the solid phase is less than or equal to a given number; see [39] for more details. Figure 11 shows the spherical contact distribution functions of the solid phase for the simulated and experimental microstructures.

Chord length distribution functions are also important characteristics. A chord length distribution function is computed as follows. Straight lines with a fixed direction (e.g., parallel to the x -axis) are intersected with the solid phase. The chord length distribution function is the cumulative distribution function of the lengths of the resulting intersections. Figure 12 shows the chord length distribution functions for lines parallel to the x , y and z axes. All three functions are essentially identical, indicating that both the material and the stochastic model are isotropic, as expected. The chord length distribution functions of the experimental microstructures and the microstructures produced by the stochastic model are very close to one another.

As discussed in Section 3.2, the connectivity structure of the particle system is complex and difficult to model. In order to evaluate our success in this respect, we extract connectivity graphs from the experimental samples and the realizations of the stochastic model. We then consider the distributions of the coordination numbers of these graphs. The connectivity graphs are extracted from the binary images by skeletonizing the solid phases using the technique described in [48]. Each skeleton is then converted into a graph as follows. All voxels of the skeleton with more than two neighbors are treated as vertices of the graph. Likewise, all voxels with only one neighbor are treated as vertices. Two vertices are connected by an edge if they can be connected by voxels in the skeleton without passing through another vertex. The degree of a vertex is the number of neighboring vertices. The distributions of the coordination numbers are shown in Figure 13. Note the similarity between the distributions for the stochastic model and the experimental samples.

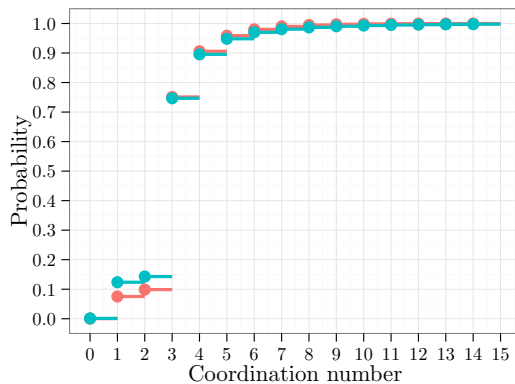


Figure 13: Distribution functions of coordination numbers of the connectivity graph. Red: experimental; blue: simulated.

4.2. Characteristics of the pore phase

The geometry of the pore space of the material plays an important role in determining the material’s functionality, as the transport of lithium ions takes place in the pores. We consider two characteristics of the pore space that are related to transport properties of the lithium-ion anode: the pore size distribution and the distribution of local tortuosities.

The pore size distribution describes the proportion of the pore phase that can be covered by spheres with a given radius. The pore size distributions of the experimental and simulated microstructures are shown in Figure 14. One can see that the curves differ for pores larger than 4 voxels. However, this difference is not too important, as local tortuosity, which we consider next, plays a far greater role in determining the transport behavior of a structure [54, 55].

The local tortuosity of the pore space of a material, defined in [54], is a characteristic describing the tortuosity of a path through the pore space from a point on the surface of the material to the closest point on the opposite surface. It is calculated by first skeletonizing the pore space. The shortest path from the point on the surface through the graph to a point on the opposite face is then calculated. If the point is not inside the pore space, the path travels along the surface of the material until it reaches the pore phase. The local tortuosity is then given by the ratio of the shortest path length to the shortest Euclidean distance from the point to the opposite surface. We consider the local tortuosities of points placed uniformly on the surfaces of the materials. The probability densities of these local tortuosities are shown in Figure 15. The tortuosity distributions of the experimental and simulated microstructures show strong accordance with one another. This indicates that the functional properties of the output of the stochastic model should resemble the functional properties of the actual materials quite closely.

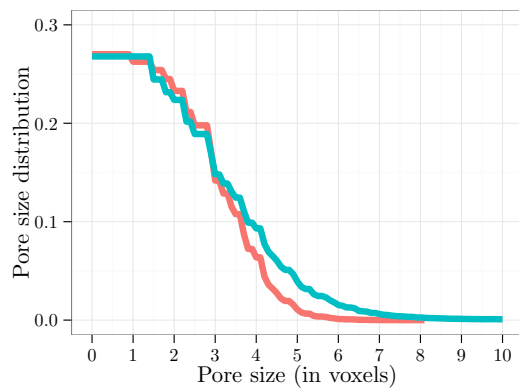


Figure 14: Pore size distributions. Red: experimental; blue: simulated.

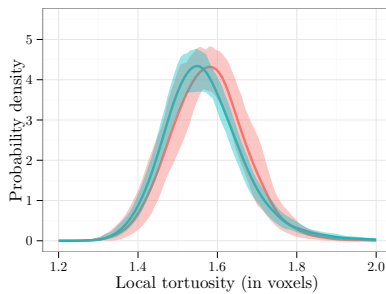


Figure 15: Probability densities of local tortuosities. Mean values are indicated by the dark lines and the ranges between the 0.05 and 0.95 quantiles are shown in lighter colors. Red: experimental; blue: simulated.

5. Summary & Outlook

In this paper, we introduced a stochastic 3D model for the microstructure of lithium-ion battery anodes. Such anodes consist of a network of connected graphite particles. The data basis for our model was four 3D images of samples extracted from a lithium-ion battery. The model itself consists of four steps. In the first step, a random tessellation is produced which roughly determines the shape and size of the particles. In the second step, a random graph is generated. This graph describes how the particles connect with one another. In the third step, the particles themselves are generated. We do this using a novel approach, based on Gaussian random fields on the sphere. In the final step, the resulting microstructure is smoothed in order to ensure that it realistically models the material.

The stochastic model was developed in order to produce a large number of virtual, but realistic, microstructures by systematic modification of model parameters. In the next stage of our research, electrochemical simulations will be carried out on these microstructures, in order to understand the relationships between various microstructure characteristics and the functionality of the material. Additionally, we will consider a number of microstructures produced using different production parameters. We will fit our model to these structures and investigate the relationship between production parameters and model parameters. This will ultimately allow us to carry out virtual materials design, where simulated structures are generated for a wide spectrum of production parameters and investigated in order to identify optimal production parameters.

Acknowledgement

This work was partially funded by BMBF under grant number 05M13VUA in the programme “Mathematik für Innovationen in Industrie und Dienstleistungen”.

- [1] A. Barré, B. Deguilhem, S. Grolleau, M. Gérard, F. Suard, D. Riu, A review on lithium-ion battery ageing mechanisms and estimations for automotive applications, *Journal of Power Sources* 241 (2013) 680–689.
- [2] P. Arora, R. E. White, M. Doyle, Capacity fade mechanisms and side reactions in lithium-ion batteries, *Journal of the Electrochemical Society* 145 (10) (1998) 3647–3667.
- [3] M. Broussely, P. Biensan, F. Bonhomme, P. Blanchard, S. Herreyre, K. Nechev, R. J. Staniewicz, Main aging mechanisms in Li ion batteries, *Journal of Power Sources* 146 (1) (2005) 90–96.
- [4] J. Fan, S. Tan, Studies on charging lithium-ion cells at low temperatures, *Journal of the Electrochemical Society* 153 (6) (2006) A1081–A1092.
- [5] J. Vetter, P. Novak, M. R. Wagner, C. Veit, K.-C. Möller, J. O. Besenhard, M. Winter, M. Wohlfahrt-Mehrens, C. Vogler, A. Hammouche, Ageing mechanisms in lithium-ion batteries, *Journal of Power Sources* 147 (1) (2005) 269–281.
- [6] A. Latz, J. Zausch, Thermodynamic consistent transport theory of Li-ion batteries, *Journal of Power Sources* 196 (6) (2011) 3296–3302.
- [7] J. Newman, K. E. Thomas, H. Hafezi, D. R. Wheeler, Modeling of lithium-ion batteries, *Journal of Power Sources* 119 (2003) 838–843.
- [8] A. F. Bower, P. R. Guduru, V. A. Sethuraman, A finite strain model of stress, diffusion, plastic flow, and electrochemical reactions in a lithium-ion half-cell, *Journal of the Mechanics and Physics of Solids* 59 (4) (2011) 804–828.
- [9] X. Zhang, W. Shyy, A. M. Sastry, Numerical simulation of intercalation-induced stress in Li-ion battery electrode particles, *Journal of the Electrochemical Society* 154 (10) (2007) A910–A916.
- [10] P. Arora, M. Doyle, R. E. White, Mathematical modeling of the lithium deposition overcharge reaction in lithium-ion batteries using carbon-based negative electrodes, *Journal of the Electrochemical Society* 146 (10) (1999) 3543–3553.
- [11] B. Y. Liaw, R. G. Jungst, G. Nagasubramanian, H. L. Case, D. H. Doughty, Modeling capacity fade in lithium-ion cells, *Journal of Power Sources* 140 (1) (2005) 157–161.
- [12] S. Tippmann, D. Walper, B. Spier, W. G. Bessler, Low-temperature charging of lithium-ion cells. Part I: Electrochemical modeling and experimental investigation on degradation behavior, *Journal of Power Sources* 252 (2014) 305–316.

- [13] C.-F. Chen, P. P. Mukherjee, Probing the morphological influence on solid electrolyte interphase and impedance response in intercalation electrodes, *Physical Chemistry Chemical Physics* 17 (15) (2015) 9812–9827.
- [14] S. Cho, C.-F. Chen, P. P. Mukherjee, Influence of microstructure on impedance response in intercalation electrodes, *Journal of the Electrochemical Society* 162 (7) (2015) A1202–A1214.
- [15] S. Cooper, D. Eastwood, J. Gelb, G. Damblanc, D. Brett, R. Bradley, P. Withers, P. D. Lee, A. Marquis, N. P. Brandon, P. R. Shearing, Image based modelling of microstructural heterogeneity in LiFePO_4 electrodes for Li-ion batteries, *Journal of Power Sources* 247 (2013) 1033–1039.
- [16] S. J. Harris, P. Lu, Effects of inhomogeneities - nanoscale to mesoscale - on the durability of Li-ion batteries, *The Journal of Physical Chemistry C* 117 (13) (2013) 6481–6492.
- [17] A. Latz, J. Zausch, O. Iliev, Modeling of species and charge transport in Li-ion batteries based on non-equilibrium thermodynamics, in: I. Dimov, S. Dimova, N. Kolkovska (Eds.), *Numerical Methods and Applications*, Vol. 6046 of *Lecture Notes in Computer Science*, Springer, 2011, pp. 329–337.
- [18] V. Ramadesigan, P. W. Northrop, S. De, S. Santhanagopalan, R. D. Braatz, V. R. Subramanian, Modeling and simulation of lithium-ion batteries from a systems engineering perspective, *Journal of the Electrochemical Society* 159 (3) (2012) R31–R45.
- [19] S. H. Kim, H. Pitsch, Reconstruction and effective transport properties of the catalyst layer in PEM fuel cells, *Journal of the Electrochemical Society* 156 (6) (2009) B673–B681.
- [20] N. Siddique, F. Liu, Process based reconstruction and simulation of a three-dimensional fuel cell catalyst layer, *Electrochimica Acta* 55 (19) (2010) 5357–5366.
- [21] D. Eastwood, P. Bayley, H. Chang, O. Taiwo, J. Vila-Comamala, D. Brett, C. Rau, P. Withers, P. R. Shearing, C. Grey, P. D. Lee, Three-dimensional characterization of electrodeposited lithium microstructures using synchrotron X-ray phase contrast imaging, *Chemical Communications* 51 (2) (2015) 266–268.
- [22] D. Eastwood, R. Bradley, F. Tariq, S. Cooper, O. Taiwo, J. Gelb, A. Merkle, D. Brett, N. P. Brandon, P. Withers, P. D. Lee, P. R. Shearing, The application of phase contrast X-ray techniques for imaging Li-ion battery electrodes, *Nuclear Instruments and Methods in Physics Research Section B: Beam Interactions with Materials and Atoms* 324 (2014) 118–123.
- [23] T. Mitsch, Y. Krämer, J. Feinauer, G. Gaiselmann, H. Markötter, I. Manke, A. Hintennach, V. Schmidt, Preparation and characterization of Li-ion

- graphite anodes using synchrotron tomography, *Materials* 7 (6) (2014) 4455–4472.
- [24] P. R. Shearing, Y. Wu, S. J. Harris, N. Brandon, In situ X-ray spectroscopy and imaging of battery materials, *Interface-Electrochemical Society* 20 (3) (2011) 43.
- [25] F. Tariq, V. Yufit, M. Kishimoto, P. R. Shearing, S. Menkin, D. Golodnitsky, J. Gelb, E. Peled, N. P. Brandon, Three-dimensional high resolution X-ray imaging and quantification of lithium ion battery mesocarbon microbead anodes, *Journal of Power Sources* 248 (2014) 1014–1020.
- [26] G. Teixidor, B. Park, P. P. Mukherjee, Q. Kang, M. J. Madou, Modeling fractal electrodes for Li-ion batteries, *Electrochimica Acta* 54 (24) (2009) 5928–5936.
- [27] W. Wu, F. M. Jiang, Simulated annealing reconstruction and characterization of a LiCoO_2 Lithium-ion battery cathode, *Chinese Science Bulletin* 58 (36) (2013) 4692–4695.
- [28] W. Wu, F. M. Jiang, Microstructure reconstruction and characterization of PEMFC electrodes, *International Journal of Hydrogen Energy* 39 (28) (2014) 15894–15906.
- [29] L. Zielke, T. Hutzenlaub, D. R. Wheeler, I. Manke, T. Arlt, N. Paust, R. Zengerle, S. Thiele, A combination of X-ray tomography and carbon binder modeling: Reconstructing the three phases of LiCoO_2 Li-ion battery cathodes, *Advanced Energy Materials* 4 (8) (2014) 1301617.
- [30] L. Zielke, T. Hutzenlaub, D. R. Wheeler, C.-W. Chao, I. Manke, A. Hilger, N. Paust, R. Zengerle, S. Thiele, Three-phase multiscale modeling of a LiCoO_2 cathode: Combining the advantages of FIB-SEM imaging and X-ray tomography, *Advanced Energy Materials* 5 (5) (2014) 1401612.
- [31] G. Gaiselmann, R. Thiedmann, I. Manke, W. Lehnert, V. Schmidt, Stochastic 3D modeling of fiber-based materials, *Computational Materials Science* 59 (2012) 75–86.
- [32] O. Stenzel, L. Koster, R. Thiedmann, S. D. Oosterhout, R. A. J. Janssen, V. Schmidt, A new approach to model-based simulation of disordered polymer blend solar cells, *Advanced Functional Materials* 22 (2012) 1236–1244.
- [33] O. Stenzel, D. Westhoff, I. Manke, M. Kasper, D. P. Kroese, V. Schmidt, Graph-based simulated annealing: a hybrid approach to stochastic modeling of complex microstructures, *Modelling and Simulation in Materials Science and Engineering* 21 (5) (2013) 055004.
- [34] R. Thiedmann, O. Stenzel, A. Spettl, P. R. Shearing, S. J. Harris, N. P. Brandon, V. Schmidt, Stochastic simulation model for the 3D morphology of composite materials in Li-ion batteries, *Computational Materials Science* 50 (12) (2011) 3365–3376.

- [35] D. Westhoff, J. J. van Franeker, T. Brereton, D. P. Kroese, R. A. J. Janssen, V. Schmidt, Stochastic modeling and predictive simulations for the microstructure of organic semiconductor films processed with different spin coating velocities, *Modelling and Simulation in Materials Science and Engineering* 23 (4) (2015) 045003.
- [36] G. Gaiselmann, M. Neumann, O. Pecho, T. Hocker, V. Schmidt, L. Holzer, Quantitative relationships between microstructure and effective transport properties based on virtual materials testing, *AIChE Journal* 60 (2014) 1983–1999.
- [37] M. Roland, A. Kruglova, G. Gaiselmann, T. Brereton, V. Schmidt, F. Mücklich, S. Diebels, Numerical simulation and comparison of a real Al-Si alloy with virtually generated alloys, *Archive of Applied Mechanics*.
- [38] Z. Liu, P. P. Mukherjee, Microstructure evolution in lithium-ion battery electrode processing, *Journal of the Electrochemical Society* 161 (8) (2014) E3248–E3258.
- [39] S. N. Chiu, D. Stoyan, W. S. Kendall, J. Mecke, *Stochastic Geometry and its Applications*, 3rd Edition, J. Wiley & Sons, 2013.
- [40] W. S. Kendall, I. S. Molchanov, *New Perspectives in Stochastic Geometry*, Oxford University Press, 2010.
- [41] S. Torquato, *Random Heterogeneous Materials: Microstructure and Macroscopic Properties*, Springer, 2002.
- [42] J. Feinauer, A. Spetl, I. Manke, S. Strege, A. Kwade, A. Pott, V. Schmidt, Structural characterization of particle systems using spherical harmonics, *Materials Characterization* 106 (0) (2015) 123 – 133.
- [43] G. Gaiselmann, M. Neumann, L. Holzer, T. Hocker, M. R. Prestat, V. Schmidt, Stochastic 3D modeling of LSC cathodes based on structural segmentation of FIB-SEM images, *Computational Materials Science* 67 (2013) 48–62.
- [44] G. B. Arfken, H. J. Weber, *Mathematical Methods for Physicists*, 5th Edition, Harcourt Academic Press, 2001.
- [45] L. Shapiro, G. C. Stockman, *Computer Vision*, Prentice Hall, 2001.
- [46] S. Beucher, Watershed, hierarchical segmentation and waterfall algorithm, in: P. Soille, M. Pesaresi, G. Ouzounis (Eds.), *Mathematical Morphology and its Applications to Image Processing*, Springer, 1994, pp. 69–76.
- [47] J. Hoshen, R. Kopelman, Percolation and cluster distribution. I. Cluster multiple labeling technique and critical concentration algorithm, *Phys. Rev. B* 14 (1976) 3438–3445.

- [48] T.-C. Lee, R. L. Kashyap, C.-N. Chu, Building skeleton models via 3-D medial surface axis thinning algorithms, *CVGIP: Graphical Models and Image Processing* 56 (6) (1994) 462–478.
- [49] S. Beucher, C. Lantuéjoul, Use of watersheds in contour detection, in: *Proceedings of the International Workshop on Image Processing, Real-Time Edge and Motion Detection/Estimation*, Rennes, France, 1979.
- [50] S. Beucher, F. Meyer, The morphological approach to segmentation: the watershed transformation, in: E. Dougherty (Ed.), *Mathematical Morphology in Image Processing*, Marcel Dekker, 1993, pp. 433–481.
- [51] A. Spettl, R. Wimmer, T. Werz, M. Heinze, S. Odenbach, C. E. Krill III, V. Schmidt, Stochastic 3D modeling of Ostwald ripening at ultra-high volume fractions of the coarsening phase, *Modelling and Simulation in Materials Science and Engineering* (in print).
- [52] C. Lautensack, Random laguerre tessellations, Ph.D. thesis, Universität Karlsruhe (TH) (2007).
- [53] J. Møller, Random tessellations in \mathbb{R}^d , *Advances in Applied Probability* 21 (1) (1989) 37–73.
- [54] R. Thiedmann, C. Hartnig, I. Manke, V. Schmidt, W. Lehnert, Local structural characteristics of pore space in GDLs of PEM fuel cells based on geometric 3D graphs, *Journal of the Electrochemical Society* 156 (11) (2009) B1339–B1347.
- [55] R. Thiedmann, I. Manke, W. Lehnert, V. Schmidt, Random geometric graphs for modelling the pore space of fibre-based materials, *Journal of Materials Science* 46 (24) (2011) 7745–7759.
- [56] A. Lang, C. Schwab, Isotropic Gaussian random fields on the sphere: regularity, fast simulation, and stochastic partial differential equations, *Annals of Applied Probability*.
- [57] D. Marquardt, An algorithm for least-squares estimation of nonlinear parameters, *SIAM Journal on Applied Mathematics* 11 (2) (1963) 431–441.
- [58] E. Dougherty (Ed.), *Mathematical Morphology in Image Processing*, Optical Science and Engineering, Taylor & Francis, 1992.